

## Research Paper

## Investigation of local soil resistance on suction caissons at capacity in undrained clay under combined loading

Stephen K. Suryasentana<sup>a,\*</sup>, Harvey J. Burd<sup>b</sup>, Byron W. Byrne<sup>b</sup>, Avi Shonberg<sup>c</sup><sup>a</sup> Department of Civil and Environmental Engineering, University of Strathclyde, Glasgow, UK<sup>b</sup> Department of Engineering Science, University of Oxford, Oxford, UK<sup>c</sup> Ørsted Wind Power, London, UK

## ARTICLE INFO

## Keywords:

Bearing capacity  
Failure  
Foundations  
Soil-structure interaction  
Offshore engineering  
Numerical modelling

## ABSTRACT

Winkler modelling offers a flexible and computationally efficient framework for estimating suction caisson capacity. However, there is a limited understanding of the local soil resistance acting on caissons at capacity under combined six degrees-of-freedom (6DoF) loading, which is essential for accurately estimating caisson failure envelopes. Furthermore, existing simplified design models for caissons cannot assess capacity under non-planar lateral and moment loading, which is common in offshore wind applications. To address these limitations, this paper presents a comprehensive three-dimensional (3D) finite element analysis (FEA) study, which investigates the local soil resistance acting on the caisson at capacity in undrained clay under combined 6DoF loading. The paper introduces the concept of 'soil reaction failure envelopes' to characterise the interactions between soil reactions at capacity. Closed-form formulations are derived to approximate these soil reaction failure envelopes. An elastoplastic Winkler model is then developed, incorporating linear elastic perfectly plastic soil reactions based on these formulations. The results demonstrate that the Winkler model can provide efficient and reasonably accurate estimations of caisson capacity under combined 6DoF loading, even for irregular soil profiles that pose much uncertainty and challenges to existing macro-element models.

## 1. Introduction

Offshore wind energy is expected to grow rapidly over the next few decades, following ambitious renewable energy targets set by countries worldwide. To support this growth in offshore wind energy generation, offshore wind farms are moving into deeper waters, where traditional foundations such as monopiles are gradually being replaced by more cost-effective foundations such as jacket structures on suction caissons or floating wind platforms anchored by suction caissons. For example, jacket structures on suction caissons were recently deployed at several offshore windfarms: Borkum Riffgrund 1 in 2014, Aberdeen Bay in 2018 and Seagreen in 2021. Suction caisson anchors were also recently deployed for floating wind turbines at the Hywind offshore wind farm in 2017. Suction caissons (or suction buckets) are attractive as they can be installed faster, quieter and cheaper than monopiles, which brings about significant cost advantages and environmental benefits such as reduced noise pollution.

While there are several simplified design models for estimating the

stiffnesses of suction caissons (e.g. He et al., 2017; Jalbi et al., 2018; Efthymiou and Gazetas, 2019), including some that consider the full six degrees of freedom (6DoF) load space (e.g. Doherty et al., 2005; Suryasentana et al., 2017, 2022, 2023a,b), the available simplified design models for estimating the ultimate capacity of suction caissons under combined loading are more limited. In particular, existing models for estimating caisson capacity are only applicable to planar *HM* loading (where *H* and *M* represent the lateral and moment loads, respectively). Planar *HM* loading refers to loading conditions where the lateral and moment loads are in the 'same plane', or specifically when the moment vector is orthogonal to the lateral load vector. There is currently no model for estimating the caisson capacity under non-planar *HM* loading, which is common in offshore wind applications due to different directions of wind and wave actions. It is worth noting that such models exist for other foundation types, e.g. surface foundations (Shen et al., 2017; Suryasentana et al., 2021) and mudmat foundations (Feng et al., 2014a,b; Feng and Gourvenec, 2015; Feng et al., 2015).

The failure envelope approach is widely used to assess the ultimate capacity of shallow foundations under combined loading, as recom-

\* Corresponding author.

E-mail addresses: [stephen.suryasentana@strath.ac.uk](mailto:stephen.suryasentana@strath.ac.uk) (S.K. Suryasentana), [harvey.burd@eng.ox.ac.uk](mailto:harvey.burd@eng.ox.ac.uk) (H.J. Burd), [byron.byrne@eng.ox.ac.uk](mailto:byron.byrne@eng.ox.ac.uk) (B.W. Byrne), [avish@orsted.com](mailto:avish@orsted.com) (A. Shonberg).

<https://doi.org/10.1016/j.compgeo.2024.106241>

Received 27 October 2023; Received in revised form 28 February 2024; Accepted 13 March 2024

Available online 19 March 2024

0266-352X/© 2024 The Author(s). Published by Elsevier Ltd. This is an open access article under the CC BY license (<http://creativecommons.org/licenses/by/4.0/>).

Nomenclature			
$V$	vertical load	$h_0$	horizontal soil reaction uniaxial capacity
$H_x$	horizontal load along x-axis	$m_0$	moment soil reaction uniaxial capacity
$H_y$	horizontal load along y-axis	$q_0$	torsion soil reaction uniaxial capacity
$M_x$	moment about x-axis	$\tilde{v}$	normalised vertical soil reaction
$M_y$	moment about y-axis	$\tilde{h}_x$	normalised horizontal soil reaction along x-axis
$Q$	torque about z-axis	$\tilde{h}_y$	normalised horizontal soil reaction along y-axis
$V_0$	vertical uniaxial capacity	$\tilde{m}_x$	normalised moment soil reaction about x-axis
$H_0$	horizontal uniaxial capacity	$\tilde{m}_y$	normalised moment soil reaction about y-axis
$M_0$	moment uniaxial capacity	$\tilde{q}$	normalised torque soil reaction about z-axis
$Q_0$	torsion uniaxial capacity	$h_i$	horizontal soil reaction along a general axis $i$ in the x-y plane
$\tilde{V}$	normalised vertical load	$m_j$	moment soil reaction about a general axis $j$ in x-y plane
$\tilde{H}_x$	normalised horizontal load along x-axis	$\tilde{h}_i$	normalised horizontal soil reaction along a general axis $i$ in x-y plane
$\tilde{H}_y$	normalised horizontal load along y-axis	$\tilde{m}_j$	normalised moment soil reaction about a general axis $j$ in x-y plane
$\tilde{M}_x$	normalised moment about x-axis	$s_u$	undrained shear strength
$\tilde{M}_y$	normalised moment about y-axis	$L$	suction caisson embedded length
$\tilde{Q}$	normalised torque about z-axis	$D$	suction caisson diameter
$H_i$	horizontal load along a general axis $i$ in the x-y plane	$f^{\text{skirt}}$	local failure envelope formulation for skirt soil reactions
$M_j$	moment about a general axis $j$ in x-y plane	$f^{\text{base}}$	local failure envelope formulation for base soil reactions
$\tilde{H}_i$	normalised horizontal load along a general axis $i$ in x-y plane	$\alpha_{\text{se}}$	angle between the horizontal displacement direction and the normal to the rotation axis
$\tilde{M}_j$	normalised moment about a general axis $j$ in x-y plane	$\alpha_{HM}$	angle between $H_i$ axis and $M_j$ axis (which is clockwise orthogonal to $M_j$ axis)
$U_x, U_y, U_z$	displacements in the x, y and z directions	$\alpha_{hm}$	angle between $h_i$ axis and $m_j$ axis (which is clockwise orthogonal to $m_j$ axis)
$\Theta_x, \Theta_y, \Theta_z$	rotations about the x, y and z axes	$A^{\text{skirt}}$	external surface area of the caisson skirt per metre skirt length, equivalent to $\pi D$
$v$	vertical soil reaction	$A^{\text{base}}$	area of the caisson base, equivalent to $\pi D^2/4$
$h_x$	horizontal soil reaction along x-axis	$p_{\text{atm}}$	atmospheric pressure
$h_y$	horizontal soil reaction along y-axis		
$m_x$	moment soil reaction about x-axis		
$m_y$	moment soil reaction about y-axis		
$q$	torque soil reaction about z-axis		
$v_0$	vertical soil reaction uniaxial capacity		

mended by several design guidelines (e.g. Paikowsky, 2010; API, 2011; ISO, 2016; Offshore Wind Accelerator, 2019). A failure envelope defines the combination of loads that cause an ultimate limit state of a foundation and is typically represented by a mathematical formulation that provides a reasonably good fit with failure load data generated by numerical and/or experimental studies. With reference to the caisson configuration in Fig. 1a, a failure envelope under 6DoF loading is typically represented by  $f(H_x, M_y, H_y, M_x, V, Q) = 0$ , where  $H_x, M_y, H_y, M_x, V, Q$  refer to the applied lateral force (along x-axis), rotational moment (about y-axis), lateral force (along y-axis), rotational moment (about x-axis), vertical force and torsion respectively. In this paper,  $\tilde{H}_x, \tilde{M}_y, \tilde{H}_y, \tilde{M}_x, \tilde{V}, \tilde{Q}$  refer to normalised forces or moments where  $\tilde{H}_x = H_x/H_0$ ,  $\tilde{M}_y = M_y/M_0$ ,  $\tilde{H}_y = H_y/H_0$ ,  $\tilde{M}_x = M_x/M_0$ ,  $\tilde{V} = V/V_0$ ,  $\tilde{Q} = Q/Q_0$  and  $H_0, M_0, V_0, Q_0$  are the respective uniaxial capacities. The applied loads are applied with reference to a loading reference point (LRP).

### 1.1. Existing failure envelopes for suction caissons

The initial research on evaluating the failure envelopes of suction caissons can be traced back to studies on skirted strip foundations, which can be considered as plane strain versions of suction caissons. Bransby and Randolph (1998, 1999), Bransby and Yun (2009), and Gourvenec and Barnett (2011) conducted plane-strain finite element analyses on skirted strip foundations in undrained clay under planar vertical, lateral, and moment (VHM) loading conditions. Based on their respective findings, they proposed failure envelope formulations. Subsequently, Vulpe (2015) and Hung and Kim (2014) performed three-dimensional (3D)

finite element analysis (FEA) studies on failure envelopes for suction caissons in undrained clay, considering planar VHM loading conditions. Additionally, Liu et al. (2023) conducted 3D FEA studies on the failure envelopes for suction caissons in normally consolidated undrained clay under planar vertical, lateral, moment, and torsional (VHMQ) loading conditions.

### 1.2. Winkler models

Recently, there has been growing interest in using a Winkler modelling approach to analyse the behaviour of suction caissons, similar to the approach used for piles (e.g., Byrne et al., 2020a,b; Suryasentana and Lehane, 2014a,b,2016). This approach involves representing the soil resistance through independent local soil reactions that act along the length of the caisson skirt and at its base. Typically, there are two types of soil reactions that are considered: (a) Skirt soil reactions: These are distributed soil reactions that act along the length of the caisson skirt. These reactions represent the net force or moment exerted by the soil on the cross section of the caisson per metre of skirt length; (b) Base soil reactions: These are concentrated soil reactions that act on the caisson base. These reactions represent the net force or moment exerted by the soil on the caisson base. Fig. 1c shows a schematic diagram illustrating these soil reactions.

Suryasentana et al. (2022) proposed a Winkler model (called OxCaisson) to estimate the caisson stiffness under 6DoF loading conditions in both homogeneous and non-homogeneous linear elastic soil. This model can represent a suction caisson as either fully rigid or with a flexible skirt, using one-dimensional (1D) finite element frame elements

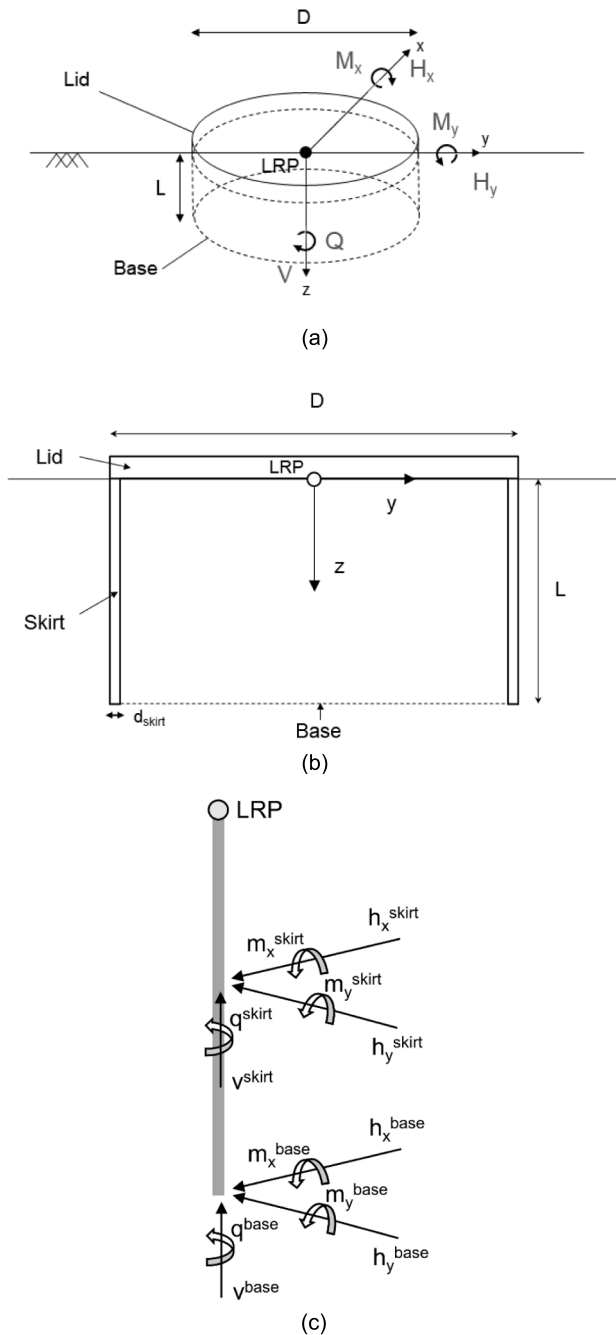


**Fig. 1.** (a) 6DoF loading configuration for suction caisson foundation, consistent with the conventions in Butterfield et al. (1997). The loading reference point (LRP) is at the centre of the foundation base. (b) Plan view of a suction caisson foundation embedded in the ground. (c) Schematic diagram of a one-dimensional Winkler model for a suction caisson foundation, which is subjected to distributed ‘skirt soil reactions’ along its skirt (with the figure illustrating a single example at a specific depth) and concentrated ‘base soil reactions’ at the base of the caisson.

(in which shear and bending in the skirts is represented by Timoshenko beam theory). The formulations for the linear elastic soil reactions of OxCaisson were derived from 3D FEA calibration results. Antoniou et al. (2022) proposed a ‘Caisson-on-Winkler-Soil’ (CWS) model for performance-based seismic design of suction caissons under planar *VHM* loading. The soil reactions in this model are represented by ‘hysteretic elements’ that are also calibrated using 3D FEA. Each hysteretic element has an ultimate strength for each load direction, which contributes to the

ultimate capacity of the caisson. Similar to the soil reactions in pile Winkler models, the ultimate strengths of the hysteretic elements are uncoupled (i.e. there is no effect of vertical loading on the ultimate lateral strength, and vice versa).

Winkler models offer several advantages over macro-element or force-resultant models. They provide a degree of separation between the structural properties of the caisson and the soil properties, allowing for more flexible modelling. Additionally, Winkler models allow direct modelling of caisson performance in ‘irregular’ soil profiles that deviate from idealised soil profiles. These advantages have been demonstrated for caisson stiffness estimations (Suryasentana et al., 2022,2023a), but they have not been shown for caisson capacity estimations. One of the main challenges in developing Winkler models for capacity estimation is the need to account for interaction between local soil reactions at capacity. Neglecting this interaction would prevent accurate reproduction of key failure envelope characteristics observed in caissons, such as the reduction in lateral capacity with increasing vertical load. Moreover, there is a lack of research on the local soil resistance acting on a caisson at capacity under combined 6DoF loading. Such research would provide valuable scientific insights into the interactions between soil reactions when the caisson is at capacity, and the contributions of the skirt and base soil reactions to the caisson capacity.

### 1.3. Objectives

The main aim of this paper is to examine the local soil resistance acting on suction caissons when they are at capacity in undrained clay under combined 6DoF loading. This is achieved by carrying out a comprehensive 3D FEA study of the ultimate suction caisson behaviour in undrained clay under 6DoF loading. Another goal is to develop a simplified design model that can predict the caisson capacity under non-planar *HM* loading. This model will facilitate routine capacity assessments for offshore wind applications, where such loading conditions are typical. Additionally, the caisson capacity for suction caisson anchor applications can be influenced by torsional loading. To this end, this paper will develop an elastoplastic Winkler model called OxCaisson-LEPP (Linear Elastic Perfectly Plastic) that can estimate the caisson capacity in undrained clay under combined 6DoF loading. OxCaisson-LEPP uses elastoplastic soil reactions derived from calibration results obtained through 3D FEA. These soil reactions are coupled to capture their interactions at capacity. As a result, OxCaisson-LEPP can estimate realistic failure envelope characteristics, including reduced lateral capacity under increased vertical loading (see Fig. 2). The advantage of the Winkler modelling approach adopted in this study is demonstrated by comparing OxCaisson-LEPP to a comparable macro-element model. Using an irregular undrained shear strength profile from a real-world case study, OxCaisson-LEPP provides more accurate estimations of the caisson failure envelope. Notably, this accuracy is achieved despite the significant differences between the irregular undrained shear strength profile used in the case study and the undrained shear strength profile used in the calibration.

## 2. Methodology

This section describes the 3D FEA study that was performed using the finite element software Abaqus v6.13 (Dassault Systèmes, 2014) to determine the capacity of a suction caisson foundation in undrained clay under combined 6DoF loading. The 3D FEA model consists of a rigid suction caisson of diameter  $D$  and skirt thickness  $d_{skirt}/D = 0.005$  on homogeneous, elastoplastic soil. The foundation diameter  $D$  was held constant at unit length, while five skirt lengths ( $L/D = 0.125, 0.25, 0.5, 1, 2$ ) were analysed. The diameter and depth of the mesh domain were set to  $6D$  and  $2L + 2.5D$  respectively. This domain size is sufficiently large to avoid significant boundary effects on the computed failure loads, as the maximum change in the uniaxial capacities of the foundation was about 0.2 % when the domain was doubled (i.e. diameter of  $12D$  and depth of

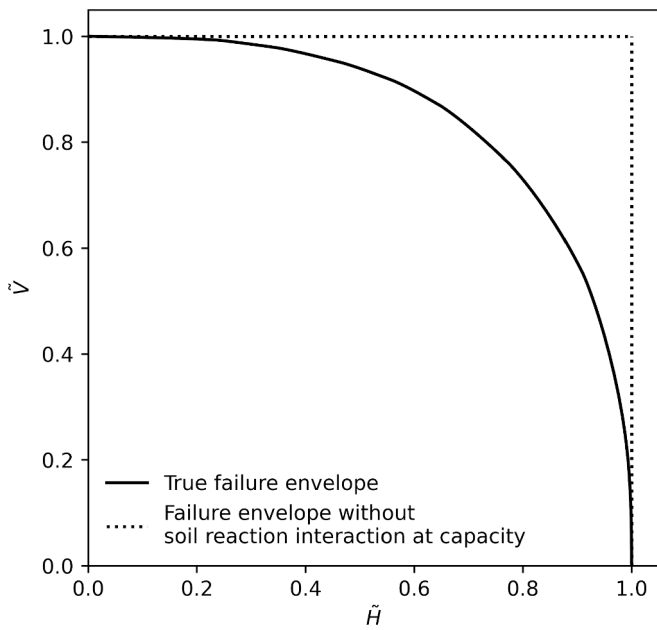


Fig. 2. Comparison of the true normalised  $VH$  failure envelope for a caisson of  $L/D = 1$ , with the corresponding failure envelope estimated by a Winkler model with soil reactions that have no interaction at capacity.

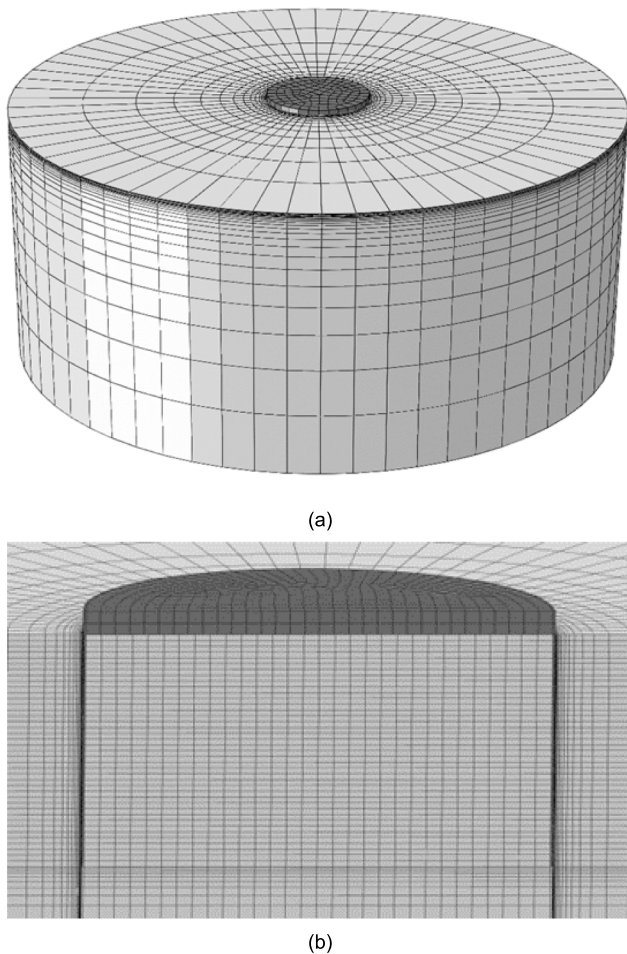


Fig. 3. (a) Oblique view of the full 3D FEA model. The diameter and depth of the mesh domain are  $6D$  and  $2L + 2.5D$  respectively. (b) Partial view of the suction caisson.

$4L + 5D$ ). A representative mesh is shown in Fig. 3.

The soil was defined as a homogeneous, isotropic linear elastic, perfectly plastic material, with uniform undrained shear strength  $s_u$ , adopting a fully-associated von Mises yield criterion. The Poisson's ratio  $\nu$  of the soil was set to 0.49, while its Young's modulus  $E$  was set to  $1000\sqrt{3} s_u$ . First-order, fully-integrated, linear, brick elements C3D8H were adopted for the soil. The caisson was modelled as a weightless, rigid body (using rigid body constraints), and the LRP was set at the centre of its lid base, as shown in Fig. 1. Separation and slip at the soil-foundation interface was prevented using tie constraints; this means that the contact interaction between the soil and the caisson skirt/lid are based on connected nodes.

## 2.1. Numerical procedures to determine failure load data

The applied loading conditions are identical to those described in Suryasentana et al. (2021); these are briefly described below. First, the uniaxial load capacities ( $Q_0$ ,  $V_0$ ,  $H_0$ ,  $M_0$ ) of the foundation were computed; note that the vertical uniaxial capacities computed apply to both compressive and tensile capacity as the finite element nodes between soil and caisson structure are connected and the employed von Mises soil model is not pressure dependent. Table 1 provides comparisons between some of the 3D FEA uniaxial load capacity results from this study and the 3D finite element limit analysis (FELA) results from Suryasentana et al., (2020b). The 3D FEA results generally agree well with these previous solutions. Next, failure envelope data were determined using combined displacement and load controls. Specifically,  $Q$  and/or  $V$  loads were first applied on the foundation, before  $HM$  contours of the failure envelope are explored by applying horizontal displacements and rotations using the sequential swipe test described in Suryasentana et al., (2020b). The values of the normalised torque and vertical load applied in the current study are  $\tilde{Q} = 0, 0.25, 0.5, 0.75$  and  $\tilde{V} = 0, 0.25, 0.5, 0.75$ . Similar to Suryasentana et al. (2021), the sequential swipe tests were applied at five different angles ( $\alpha_{SE} = 0, \pi/8, \pi/4, 3\pi/8, \pi/2$ ) between the direction of the horizontal displacement and the normal to the rotation axis (see Fig. 4a), which was sufficient to map the  $HM$  contours of the failure envelope for both planar and non-planar  $HM$  loading.  $\alpha_{HM}$  is defined here as the angle between the  $H_i$  axis and the  $M_j$  axis (which is clockwise orthogonal to the  $M_j$  axis), where  $H_i$  and  $M_j$  are the resultant lateral and moment loads along some axes  $i, j$  (see Fig. 4b).  $\alpha_{HM} = 0$  corresponds to planar  $HM$  loading.

## 2.2. Local soil reactions

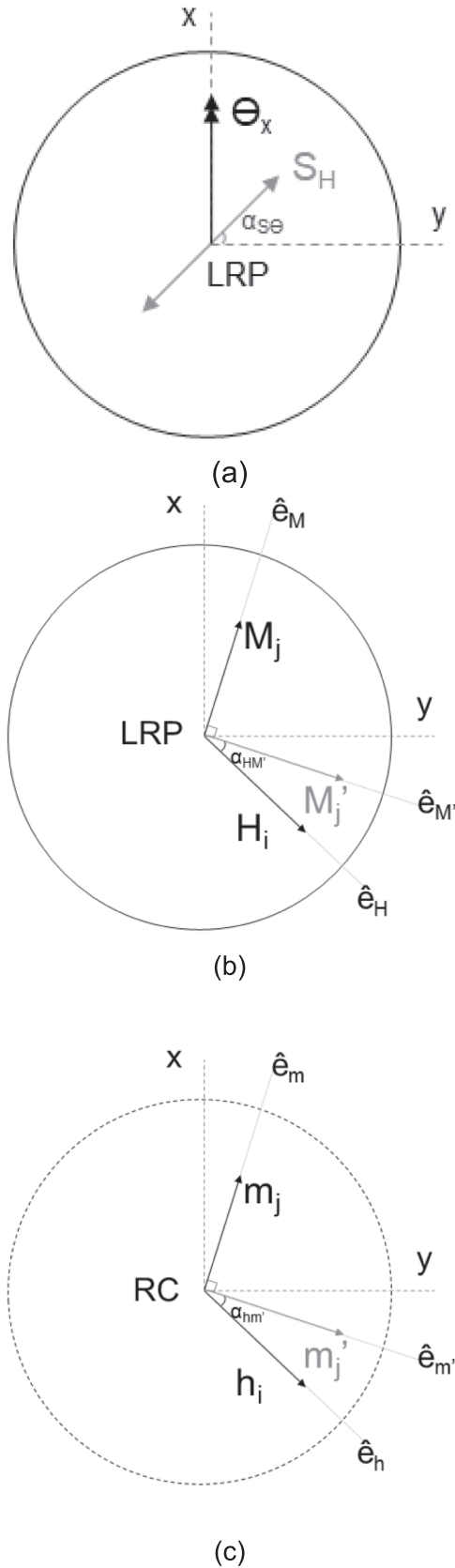
The skirt and base soil reactions are calculated from the nodal forces of the soil element nodes in contact with the caisson skirt and base respectively, as detailed in Suryasentana et al. (2022). The current study focuses on examining the values of these soil reactions and their interactions with one another when the caisson is at capacity. For the current paper,  $q_0, v_0, h_0, m_0$  are the uniaxial capacities of the torsional, vertical, lateral and moment soil reactions respectively. Consistent with their global counterparts ( $H_0, M_0, V_0, Q_0$ ), they represent the ultimate value of each soil reaction, when the other soil reactions are zero. For example,  $q_0$  is the ultimate value of  $q$ , when  $v = 0, h = 0$  and  $m = 0$ .

Table 1

Uniaxial capacities of a suction caisson of  $L/D = 1$ , where  $A = \pi D^2/4$  refers to the foundation base area.

	$\frac{L}{D}$	$\frac{Q_0}{ADs_u}$	$\frac{V_0}{As_u}$	$\frac{H_0}{As_u}$	$\frac{M_0}{ADs_u}$
3DFE	1	2.42	13.12	5.92	3.71
3D FELA (Average)	1	–	13.10	5.90	3.66
3D FELA (LB)	1	–	12.52	5.52	3.36
3D FELA (UB)	1	–	13.68	6.28	3.96
Analytical	1	2.333	–	–	–





**Fig. 4.** (a) Conventions for prescribed displacements. (b) Conventions adopted for general *HM* loading. LRP is the loading reference point of the caisson. (c) Conventions adopted for general *hm* soil reactions pointing in different relative directions. RC is the centre (and reference point) of a cross-section along the caisson skirt or at the caisson base.

Furthermore,  $\tilde{h}_i, \tilde{m}_j, \tilde{v}, \tilde{q}$  refer to normalised soil reactions where  $\tilde{h}_i = h_i/h_0$ ,  $\tilde{m}_j = m_j/m_0$ ,  $\tilde{v} = v/v_0$ ,  $\tilde{q} = q/q_0$  and  $h_i, m_j$  are the resultant lateral and moment soil reactions along some axes *i, j*.  $\alpha_{hm'}$  is defined as the angle between the  $h_i$  axis and the  $m'_j$  axis (which is clockwise orthogonal to the  $m_j$  axis), as shown in Fig. 4c.  $\alpha_{hm'}$  can be calculated as,

$$\alpha_{hm'} = \cos^{-1} \left( \frac{h_i \cdot m'_j}{h_i m_j} \right). \quad (1)$$

where  $h_i$  is the resultant lateral soil reaction vector and  $m'_j$  is a vector that is clockwise orthogonal to the resultant moment soil reaction vector  $m_j$ .

### 3. Results

The results of the 3D FEA study are mainly shown for a representative caisson of  $L/D = 0.5$ , but the findings are similar for caissons of other  $L/D$  ratios. Due to symmetry, the failure envelope results were obtained for only two quadrants.

#### 3.1. Local soil resistance on caisson at capacity

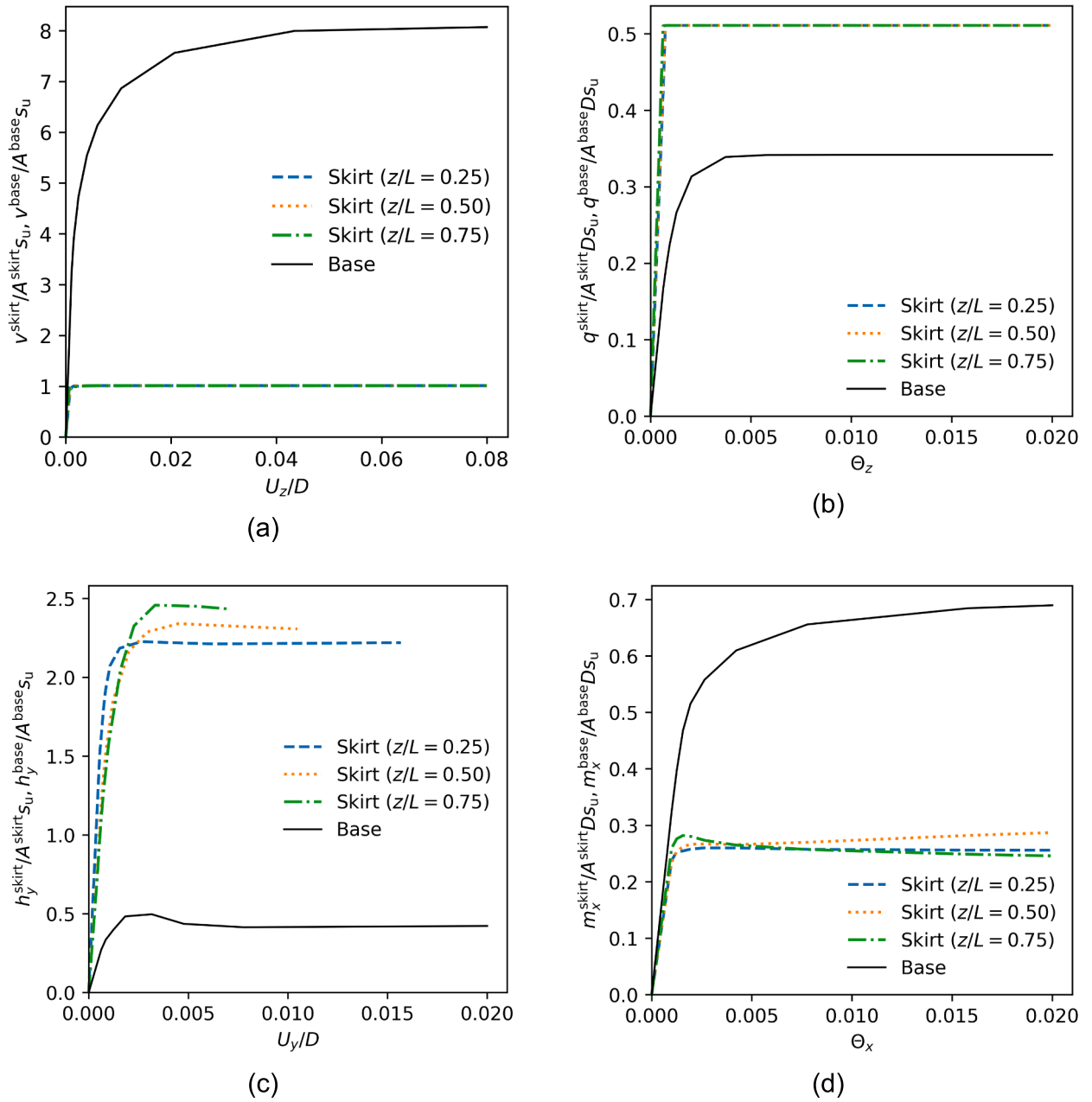
Fig. 5 shows the normalised load–displacement curves for the skirt soil reactions at various depths, as well as the base soil reaction, under various uniaxial loading conditions applied at the LRP of a caisson of  $L/D = 0.5$ , where  $U_y, U_z, \Theta_x, \Theta_z$  are the caisson lateral displacement along y-axis, vertical displacement, rotation about x-axis and torsional displacement. It can be seen that the ultimate values of the skirt soil reactions are approximately the same for all depths.

Fig. 6a illustrates the evolution of the lateral and moment skirt soil reactions at different depths as a caisson of  $L/D = 0.5$  remains at capacity, while the global load state ‘travels’ along the caisson failure envelope during a sequential swipe test in the *HM* load space for planar *HM* loading (i.e.  $\alpha_{HM} = 0$ ),  $\tilde{V} = 0, \tilde{Q} = 0$ . It can be observed that the interactions between the lateral and moment skirt reactions are broadly similar, albeit with different interaction paths at different depths. Fig. 6a also shows the interaction between the average lateral and moment skirt reactions to give an indication of the general interaction path. For better context, Fig. 6b shows the interaction paths taken by the *H* and *M* loads and the corresponding skirt (average) and base soil reactions during the sequential swipe test. The distinct interaction paths of the global loads, base soil reactions, and skirt soil reactions at caisson capacity are evident. In this paper, the interaction paths of the skirt (average) and base soil reactions are referred to as ‘skirt failure envelopes’ and ‘base failure envelopes’ respectively, for brevity.

Fig. 7 shows the variation of the skirt and base failure envelopes with increasing  $L/D$  during sequential swipe tests in the *HM* load space for planar *HM* loading,  $\tilde{V} = 0$  and  $\tilde{Q} = 0$ . It can be observed that the *hm* skirt failure envelopes get more angular in shape as  $L/D$  increases, but the shapes remain quite similar (all parallelogram-like). The *hm* base failure envelopes for  $L/D > 0$  are largely the same, but are much more rounded in shape than that for  $L/D = 0$ .

#### 3.2. Uniaxial capacities of soil reactions

Fig. 8 shows the uniaxial capacities of the skirt and base soil reactions for different  $L/D$  ratios. While the uniaxial capacities for the vertical and torsional soil reactions can be easily determined from the ultimate limiting values of the soil reactions under uniaxial loading (e.g., the limiting values from Fig. 5a and 5b), the calculations of the uniaxial capacities for the lateral and moment soil reactions are much more involved. This is because under uniaxial lateral loading (e.g., Fig. 5c), the moment soil reactions are not zero at the ultimate limiting values of the lateral soil reaction. Thus, the uniaxial capacities for the lateral and moment soil reactions are approximated as the intersection of the *hm*



**Fig. 5.** Normalised load–displacement curves of skirt soil reactions at various depths and the base soil reaction under different uniaxial loading applied at the LRP of a caisson of  $L/D = 0.5$  (a) Vertical soil reactions under purely vertical loading (b) Torsional soil reactions under pure torsion (c) Lateral soil reactions under purely lateral loading (d) Moment soil reactions under purely moment loading. Note that  $A^{base} = \frac{\pi}{4}D^2$  and  $A^{skirt} = \pi D$ .

failure envelope (e.g., Fig. 6a) with the  $h$  and  $m$  axes, respectively.

Fig. 8a shows a clear trend: as  $L/D$  increases, the lateral capacity of the caisson skirt soil reactions increases, while the vertical, moment, and torsional capacities remain relatively constant. In Fig. 8b, we observe that the vertical capacity of the caisson base soil reactions increases with  $L/D$  until it reaches a plateau after  $L/D > 1$ . On the other hand, the lateral, moment, and torsional capacities exhibit little change. These findings suggest that as  $L/D$  increases, the contribution of the skirt soil reactions to the caisson capacity becomes more significant compared to the base soil reactions. The following functions were derived to approximate the uniaxial capacities of the skirt and base soil reactions:

$$\frac{v_0^{skirt}}{A^{skirt}s_u} = 1 \quad (2)$$

$$\frac{h_0^{skirt}}{A^{skirt}s_u} = 1.73 + 1.11(1 - \exp(-0.75L/D)) \quad (3)$$

$$\frac{m_0^{skirt}}{A^{skirt}Ds_u} = 0.337 - 0.171(1 - \exp(-1.32L/D)) \quad (4)$$

$$\frac{q_0^{skirt}}{A^{skirt}Ds_u} = 0.5 \quad (5)$$

$$\frac{v_0^{base}}{A^{base}s_u} = 5.63 + 3.8(1 - \exp(-2.19L/D)) \quad (6)$$

$$\frac{h_0^{base}}{A^{base}s_u} = 1 + 0.41(1 - \exp(-2.56L/D)) \quad (7)$$

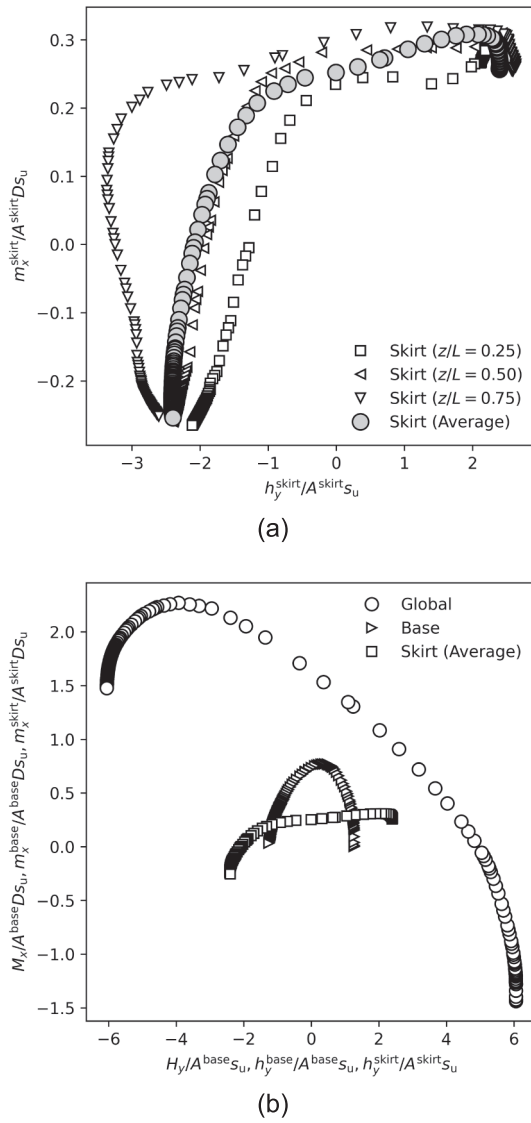


**Fig. 6.** For a sequential swipe test in the  $HM$  load space for  $\alpha_{HM} = 0, \tilde{V} = 0, \tilde{Q} = 0$ , for a caisson of  $L/D = 0.5$ : (a) Interactions between lateral and moment skirt soil reactions at various depths (b) Comparison of the caisson failure envelope with the corresponding interactions for the skirt (average) and base soil reactions during the swipe test. Note that  $A^{base} = \pi D^2/4$  and  $A^{skirt} = \pi D$ .

$$\frac{m_0^{base}}{A^{base}D_{S_u}} = 0.73 \quad (8)$$

$$\frac{q_0^{base}}{A^{base}D_{S_u}} = \frac{1}{3} \quad (9)$$

where  $A^{base} = \pi D^2/4$  is the area of the caisson base and  $A^{skirt} = \pi D$  is the external surface area of the caisson skirt per metre skirt length. The predictions of these approximating functions are also plotted in Fig. 8; evidently, they agree well with the 3D FEA calculations.

### 3.3. qvhmskirt and base failure envelopes

Figs. 9a and 10a show the effect of vertical loading on the  $hm$  contours of the skirt and base failure envelopes for a caisson of  $L/D = 0.5$ , for planar  $HM$  loading and  $\tilde{Q} = 0$ . The average  $\tilde{v}$  of all the data points in each  $hm$  contour (corresponding to a fixed  $\tilde{V}$ ) were calculated and that value is shown in the bottom left of each subfigure in Figs. 9 and 10, in

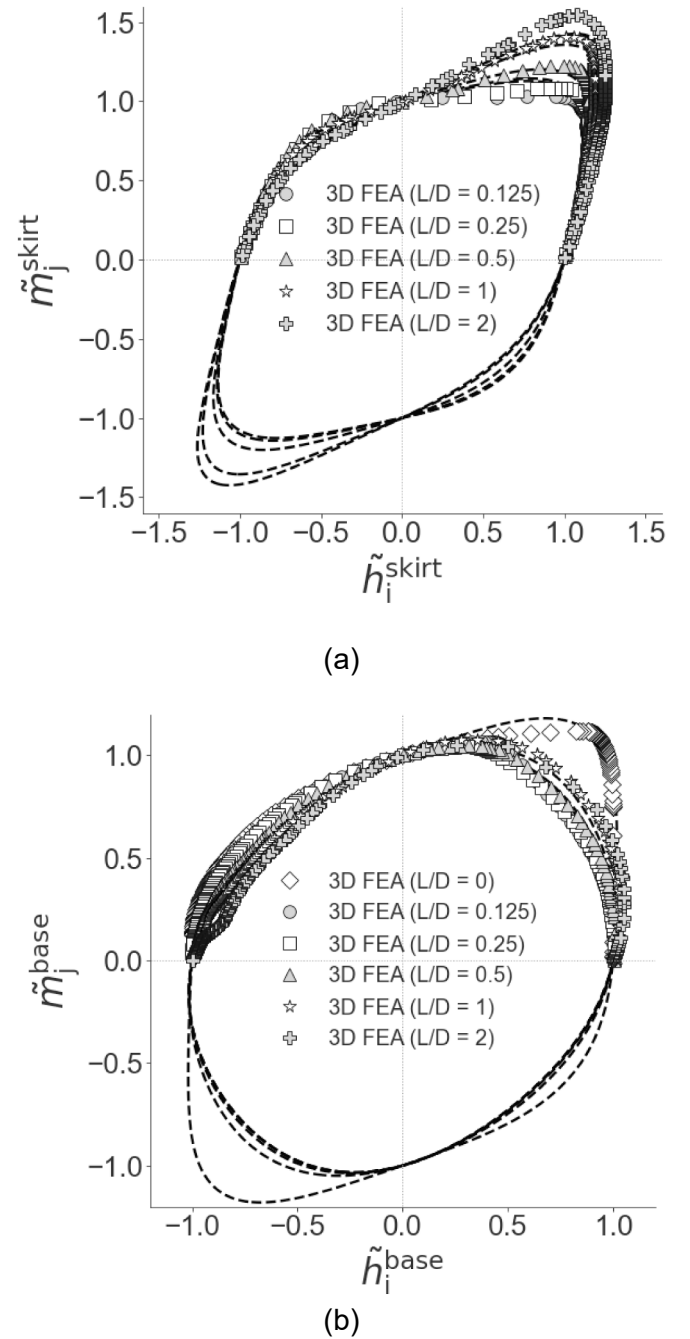


**Fig. 7.** (a) Skirt failure envelopes, and (b) base failure envelopes for caissons of various  $L/D$  ratios for  $\alpha_{HM} = 0, \tilde{V} = 0, \tilde{Q} = 0$ . The black dashed lines are the predictions of Eqs. (20) and (21).

the order of the outermost contour to the innermost. For example, in Fig. 9a,  $\tilde{V} = 0, 0.25, 0.5, 0.75$  corresponds to average  $\tilde{v} = 0, 0.06, 0.24, 0.59$  for the skirt failure envelopes. This means that when a vertical load amounting to 75% of the caisson vertical capacity is applied to the caisson during a sequential swipe test, approximately 59% of the skirt soil reaction capacities were mobilised during the test. It is evident from these figures that as  $V$  loading increases, the  $hm$  capacity for both the skirt and base soil reactions decreases, as depicted by the smaller contours. It can be observed that the drop in  $hm$  capacity is minor for  $\tilde{V} \leq 0.5$  but increases rapidly for  $\tilde{V} > 0.5$ .

Figs. 9 and 10 also show the effect of non-planar  $HM$  loading on the skirt and base failure envelopes for a caisson of  $L/D = 0.5$  and  $\tilde{Q} = 0$ .

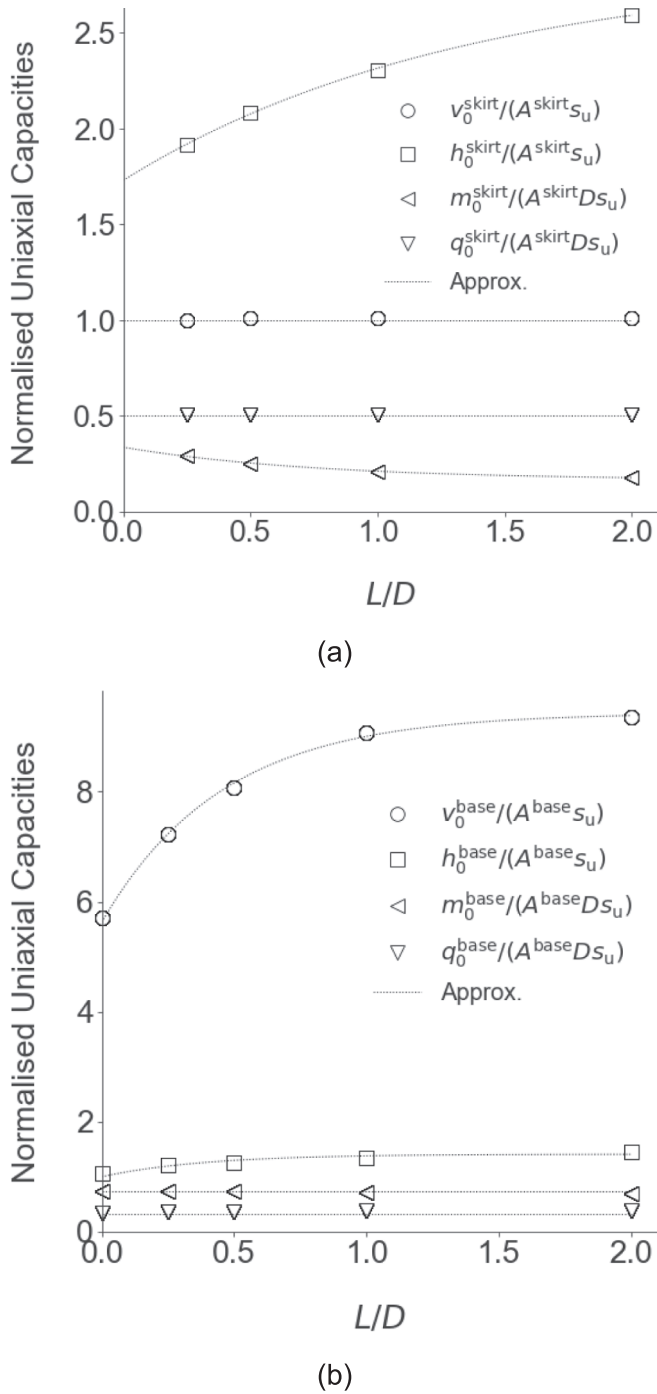


**Fig. 8.** Variation of the normalised uniaxial capacities of the skirt and base soil reactions with  $L/D$  (a) Uniaxial capacities of the skirt soil reactions (b) Uniaxial capacities of the base soil reactions. The dotted lines are the uniaxial capacities predicted by Eqs. (2)–(9).

There are much less data points for  $\alpha_{hm}' > 0$ , as the results from  $\alpha_{s\theta} = 0, \pi/4, \pi/2$  are scattered around  $0 \leq \alpha_{hm}' \leq \pi/2$ . The observable trend is that the asymmetry in the  $hm$  space decreases as  $\alpha_{hm}'$  increases from 0. Although there are few data points for  $\alpha_{hm}' = \pi/2$ , it can be shown from theoretical reasoning (see Suryasentana et al., 2021 for details) that there should not be any asymmetry at  $\alpha_{hm}' = \pi/2$ .

Fig. 11 shows the combined effects of torsional and vertical loading on the skirt and base failure envelopes for a caisson of  $L/D = 0.5$  under planar  $HM$  loading. It is evident that as torsional loading increases, the available  $hm$  capacity for both the skirt and base soil reactions decreases.

However, the shapes of the skirt and base failure envelopes remain the same as torsional loading increases. The average  $\tilde{q}$  associated with all the data points are shown at the bottom left of each subfigure in Fig. 11.

### 3.4. Elastoplastic Winkler model

The above insights into the behaviour of the soil reactions are used to develop a new simplified design model, termed 'OxCaisson-LEPP', that can predict the caisson capacity in undrained clay under 6DoF loading. OxCaisson-LEPP is an elastoplastic Winkler model that extends upon the OxCaisson model described in Suryasentana et al. (2022) to allow for linear elastic perfectly plastic (LEPP) behaviour of the soil reactions.

The elastic behaviour of the Winkler model is defined using the linear elastic soil reaction formulations described in previous works (Suryasentana et al., 2022,2023a; Suryasentana and Mayne, 2022). The proposed model combines the elastic soil reactions with plastic yield surfaces. These yield surfaces are determined by new formulations derived from the 3D FEA study, which approximates the skirt and base failure envelopes. The motivation behind adopting the Winkler modelling approach is based on the hypothesis that these soil reaction failure envelopes, calibrated at a local level, can also be applied to soil profiles different from the one used for calibration. If this hypothesis holds true, it would significantly enhance the applicability of the proposed model. The validity of the hypothesis will be assessed in a case study later in the paper.

The mechanics of the LEPP soil reactions can be explained by standard plasticity theory. For soil reaction states lying inside the yield surface, the soil response is linear elastic with the incremental response given by,

$$\delta \mathbf{b} = \mathbf{k}_e \delta \mathbf{u} \quad (10)$$

where  $\mathbf{b}$  = soil reactions vector,  $\mathbf{k}_e$  = elastic stiffness matrix for the soil reactions and  $\mathbf{u}$  = local displacements vector corresponding to the soil reactions. When the soil reaction states reach the yield surface, the soil response becomes elastoplastic, with incremental behaviour given by,

$$\delta \mathbf{b} = \mathbf{k}_{ep} \delta \mathbf{u}. \quad (11)$$

where  $\mathbf{k}_{ep}$  = elastoplastic stiffness matrix for the soil reactions. When elastoplastic yielding occurs, permanent plastic displacements accumulate with the total displacement increment  $\delta \mathbf{u}$  composed of elastic and plastic parts,

$$\delta \mathbf{u} = \delta \mathbf{u}_e + \delta \mathbf{u}_p \quad (12)$$

The elastic displacement increment  $\delta \mathbf{u}_e$  is determined through the soil reaction increment,

$$\delta \mathbf{u}_e = \mathbf{k}_e^{-1} \delta \mathbf{b} \quad (13)$$

The plastic displacement increment  $\delta \mathbf{u}_p$  is determined using the flow rule,

$$\delta \mathbf{u}_p = \lambda \frac{\partial \mathbf{g}}{\partial \mathbf{b}} \quad (14)$$

where  $\mathbf{g}(\mathbf{b})$  is a plastic potential function and  $\lambda$  is a non-negative, scalar plastic multiplier. When yielding occurs, the incremental soil reaction  $\delta \mathbf{b}$  must remain on the yield surface. This is enforced by the consistency condition,

$$\left( \frac{\partial \mathbf{f}}{\partial \mathbf{b}} \right)^T \delta \mathbf{b} = 0 \quad (15)$$

Finally,  $\mathbf{k}_{ep}$  is obtained from,



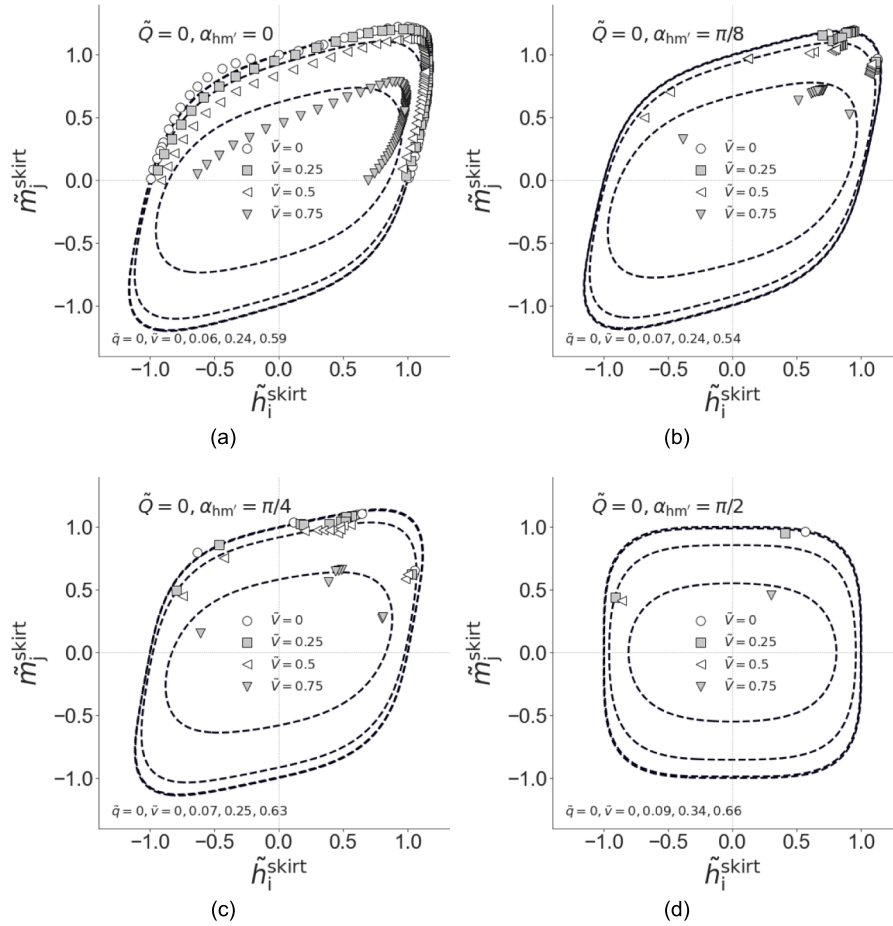


**Fig. 9.**  $hm$ Contours of skirt failure envelopes for a caisson of  $L/D = 0.5$  and for  $\alpha_{hm'} = 0, \frac{\pi}{8}, \frac{\pi}{4}, \frac{\pi}{2}$ ,  $\tilde{v} = 0, 0.25, 0.5, 0.75$ ,  $\tilde{Q} = 0$ . The black dashed lines are the skirt failure envelopes predicted by Eq. (20), while the data points are the ultimate skirt soil reactions calculated from 3D FEA. The average  $\tilde{q}$  and  $\tilde{v}$  of the data points are shown in the bottom left of each subfigure.  $\tilde{q}$  corresponds to all the data points, while  $\tilde{v}$  corresponds to the data points in each contour.

$$\mathbf{k}_{ep} = \mathbf{k}_c - \frac{\mathbf{k}_c \left( \frac{\partial \mathbf{g}}{\partial \mathbf{b}} \right) \left( \frac{\partial \mathbf{f}}{\partial \mathbf{b}} \right)^T \mathbf{k}_c}{\left( \frac{\partial \mathbf{f}}{\partial \mathbf{b}} \right)^T \mathbf{k}_c \left( \frac{\partial \mathbf{g}}{\partial \mathbf{b}} \right)} \quad (16)$$

For this paper, an associated flow rule is adopted i.e.  $\mathbf{g}(\mathbf{b}) = \mathbf{f}(\mathbf{b})$ .

OxCaisson-LEPP is implemented using a one-dimensional (1D) finite element framework, as described in Suryasentana et al. (2022). For the current study, the caisson skirt is discretised using twenty 1D skirt elements. Each skirt element is connected to a corresponding 1D soil reaction element of identical length, which represents the distributed soil reactions acting along the caisson skirt. The integration points of the soil reaction element directly use the value of the soil properties (e.g.  $s_u$ ) at the depths of the integration points.

### 3.5. Soil reaction yield surface formulations

To derive the formulations that best match the skirt and base failure envelopes determined from the 3D FEA study, the SOS-convex polynomial framework (Suryasentana et al., 2020a, 2021) is used. This framework provides an automated approach for deriving globally convex and numerically well-behaved formulations that fit failure envelope data for different foundation types and for 6DoF loading. However, the framework detailed in Suryasentana et al. (2020a, 2021) is concerned with deriving formulations for fixed failure envelopes that do not vary with foundation dimensions such as  $L/D$  ratio. The current paper extends the previous work by describing an approach for deriving 6DoF failure envelope formulations that vary with  $L/D$  and are still

guaranteed to be globally convex and numerically well-behaved.

Following the procedures in Suryasentana et al. (2021), a 4th degree homogeneous SOS-convex polynomial  $p(\alpha_{hm'}, \tilde{h}_i, \tilde{m}_j, \tilde{v}, \tilde{q})$  is sought to represent the soil reaction failure envelope  $f$  of the following form,

$$f(\alpha_{hm'}, \tilde{h}_i, \tilde{m}_j, \tilde{v}, \tilde{q}) = p(\alpha_{hm'}, \tilde{h}_i, \tilde{m}_j, \tilde{v}, \tilde{q}) - 1 = 0 \quad (17)$$

The current paper seeks to determine a soil reaction failure envelope formulation that varies with the caisson  $L/D$  ratio i.e.  $f(\frac{L}{D}, \alpha_{hm'}, \tilde{h}_i, \tilde{m}_j, \tilde{v}, \tilde{q})$ . This is not as straightforward as adding an additional input variable to the SOS-convex polynomial, i.e. replace  $p(\alpha_{hm'}, \tilde{h}_i, \tilde{m}_j, \tilde{v}, \tilde{q})$  with  $p(\frac{L}{D}, \alpha_{hm'}, \tilde{h}_i, \tilde{m}_j, \tilde{v}, \tilde{q})$  in Eq. (17). This is because global convexity is only required in the load space and not necessarily in the  $L/D$  domain. Therefore, the current paper adopts a formulation based on a convex combination of two SOS-convex polynomials ( $p_1$  and  $p_2$ ),

$$f_{LD}(\frac{L}{D}, \alpha_{hm'}, \tilde{h}_i, \tilde{m}_j, \tilde{v}, \tilde{q}) = wp_1 + (1-w)p_2 - 1 = 0 \quad (18)$$

where  $0 \leq w \leq 1$  is some weight parameter that is a function of  $L/D$ , and  $p_1$  and  $p_2$  are SOS-convex polynomials that are functions of  $\alpha_{hm'}, \tilde{h}_i, \tilde{m}_j, \tilde{v}, \tilde{q}$ . Since  $w$  and  $(1-w)$  are both non-negative,  $wp_1 + (1-w)p_2$  is convex as it is known that a non-negative weighted sum of convex functions is

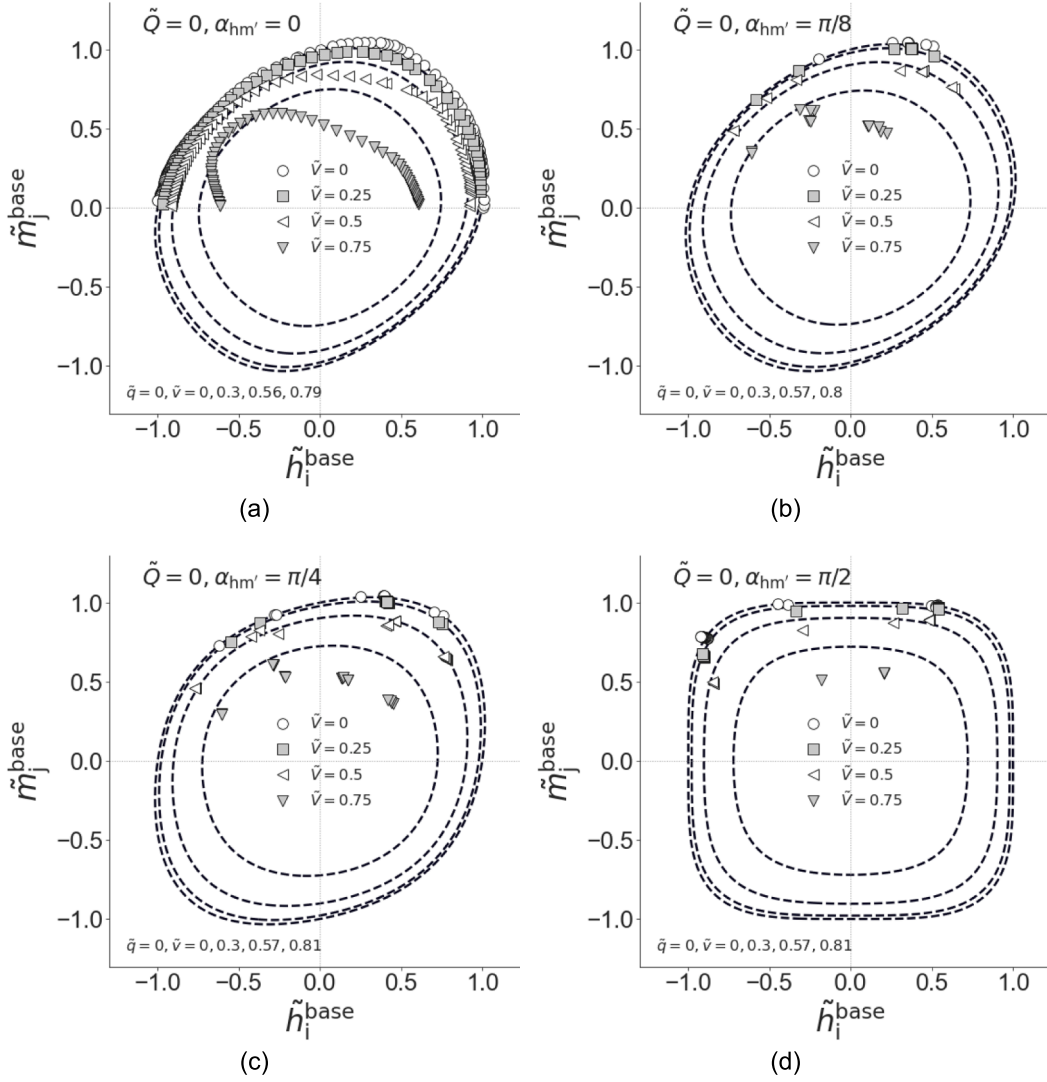


**Fig. 10.** *hm*Contours of base failure envelopes for a caisson of  $L/D = 0.5$  and for  $\alpha_{hm'} = 0, \frac{\pi}{8}, \frac{\pi}{4}, \frac{\pi}{2}$ ,  $\tilde{v} = 0, 0.25, 0.5, 0.75$ ,  $\tilde{Q} = 0$ . The black dashed lines are the base failure envelopes predicted by Eq. (21), while the data points are the ultimate base soil reactions calculated from 3D FEA. The average  $\tilde{q}$  and  $\tilde{v}$  of the data points are shown in the bottom left of each subfigure.  $\tilde{q}$  corresponds to all the data points, while  $\tilde{v}$  corresponds to the data points in each contour.

itself a convex function (Boyd and Vandenberghe, 2004). Thus, Eq. (18) is guaranteed to be globally convex as long as  $0 \leq w \leq 1$ . Further details are provided in Suryasentana and Houlsby (2022). Through an analysis of the variation of the skirt and base failure envelopes with respect to  $L/D$ ,  $w^{\text{skirt}} = \exp\left(-a\left(\frac{L}{D}\right)^2\right)$  and  $w^{\text{base}} = \exp\left(-b\left(\frac{L}{D}\right)^2\right)$  was adopted as the weight parameter functions for the skirt and base failure envelopes respectively, where  $a$  and  $b$  are unknown coefficients to be determined later. Based on these weight parameters,  $p_1$  in Eq. (18) would represent the skirt and base failure envelopes for  $L/D = 0$ , while  $p_2$  would represent the skirt and base failure envelopes as  $L/D$  approaches infinity.

To determine the unknown coefficients for the weight parameters and polynomials in Eq. (18), the skirt and base failure envelope data from the 3D FEA calculations are first transformed from the space of  $\{h_x, m_y, h_y, m_x, v, q\}$  to the standardised space of  $\{\alpha_{hm'}, \tilde{h}_i, \tilde{m}_j, \tilde{v}, \tilde{q}\}$ . The standardised data is used to determine the unknown coefficients in Eq. (18) by solving the following convex optimisation problem, which is based on the conditions: (i)  $p_1$  and  $p_2$  are both SOS-convex, and (ii) the convex combination of  $p_1$  and  $p_2$  provide a best fit with the standardised data in a 'least-squares' sense,

$$\text{minimize} \quad \sum_{i=1}^{ndata} (wp_1(\bar{x}_i^{\text{data}}) + (1-w)p_2(\bar{x}_i^{\text{data}}) - 1)^2 \quad (19)$$

subject to  $p_1$  and  $p_2$  are both SOS-convex

where  $\bar{x}_i^{\text{data}} = \{\alpha_{hm'}, \tilde{h}_i, \tilde{m}_j, \tilde{v}, \tilde{q}\}$  is a set of standardised data and  $ndata$  is the total number of data points. The MATLAB toolbox 'YALMIP' (Löfberg, 2004, 2009) was employed to solve Eq. (19) to determine the unknown coefficients.

### 3.6. Skirt and base failure envelope formulations

The skirt and base failure envelope formulations are referred to as  $f^{\text{skirt}}$  and  $f^{\text{base}}$ , respectively. They have the following functional forms based on Eq. (18),

$$f^{\text{skirt}}\left(\frac{L}{D}, \alpha_{hm'}, h_i, m_j, v, q\right) = w^{\text{skirt}} p_1^{\text{skirt}} + (1 - w^{\text{skirt}}) p_2^{\text{skirt}} - 1 = 0 \quad (20)$$

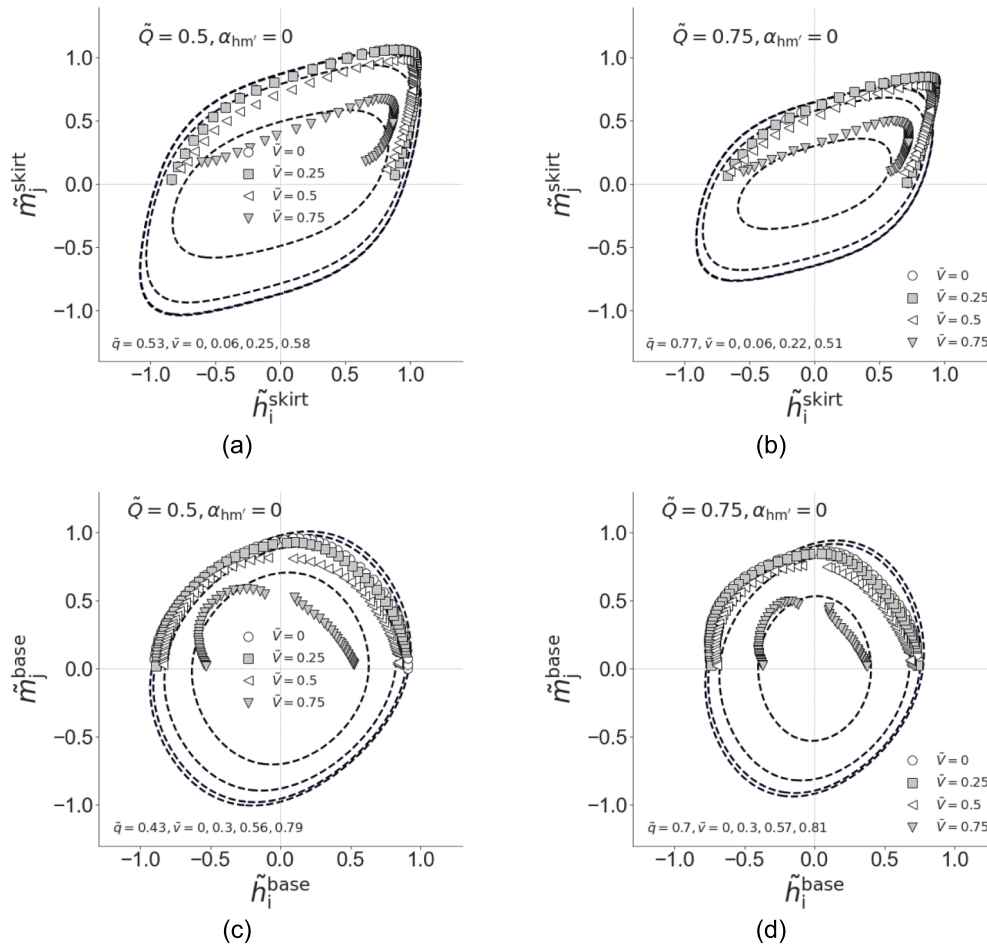


**Fig. 11.** *hm*Contours of (a) and (b) skirt failure envelopes, and (c) and (d) base failure envelopes for a caisson of  $L/D = 0.5$  and for  $\alpha_{hm} = 0$ ,  $\tilde{v} = 0, 0.25, 0.5, 0.75$ ,  $\tilde{Q} = 0.5, 0.75$ . The black dashed lines are the skirt and base failure envelopes predicted by Eqs. (20) and (21) respectively, while the data points are the ultimate soil reactions calculated from 3D FEA.

$$f^{\text{base}}\left(\frac{L}{D}, \alpha_{hm'}, h_i, m_j, v, q\right) = w^{\text{base}} p_1^{\text{base}} + (1 - w^{\text{base}}) p_2^{\text{base}} - 1 = 0 \quad (21)$$

$p_1^{\text{skirt}}, p_2^{\text{skirt}}, p_1^{\text{base}}, p_2^{\text{base}}$  all have the following functional form (but with different polynomial coefficients),

$$p\left(\alpha_{hm'}, \tilde{h}_i, \tilde{m}_j, \tilde{v}, \tilde{q}\right) = \tilde{h}_i^4 + \tilde{m}_j^4 + \tilde{v}^4 + \tilde{q}^4 + I_{hm} + I_{vh} + I_{vm} + I_{qh} + I_{qm} + I_{qv} + I_{vhm} + I_{ghm} \quad (22)$$

where

$$I_{hm} = a_1 \tilde{h}_i^2 \left( \tilde{h}_i \tilde{m}_j \cos \alpha_{hm'} \right) + a_2 \left( \tilde{h}_i \tilde{m}_j \cos \alpha_{hm'} \right)^2 + a_3 \tilde{m}_j^2 \left( \tilde{h}_i \tilde{m}_j \cos \alpha_{hm'} \right)$$

$$I_{vh} = a_4 \tilde{h}_i^2 \tilde{v}^2$$

$$I_{vhm} = a_5 \tilde{v}^2 \left( \tilde{h}_i \tilde{m}_j \cos \alpha_{hm'} \right)$$

$$I_{vm} = a_6 \tilde{m}_j^2 \tilde{v}^2$$

$$I_{qh} = a_7 \tilde{h}_i^2 \tilde{q}^2$$

$$I_{ghm} = a_8 \tilde{q}^2 \left( \tilde{h}_i \tilde{m}_j \cos \alpha_{hm'} \right)$$

$$I_{qm} = a_9 \tilde{m}_j^2 \tilde{q}^2$$

$$I_{qv} = a_{10} \tilde{v}^2 \tilde{q}^2$$

$p_1^{\text{base}}$  in Eq. (22) is the SOS-convex polynomial component of the failure envelope of a surface foundation, which is known from previous work (Suryasentana et al., 2021) and the coefficients of  $p_1^{\text{base}}$  are listed in Table 3. By solving the convex optimisation problem defined in Eq. (19), the unknown coefficients  $a_0, \dots, a_{10}$  in the interaction terms for  $p_1^{\text{skirt}}, p_2^{\text{skirt}}, p_1^{\text{base}}, p_2^{\text{base}}$  are determined and their values are listed in Tables 2 and 3 for the skirt and base failure envelopes, respectively. Furthermore, the optimised weight parameters are  $w^{\text{skirt}} = \exp\left(-2\left(\frac{L}{D}\right)^2\right)$  and  $w^{\text{base}} = \exp\left(-10\left(\frac{L}{D}\right)\right)$ .

The predictions of Eqs. (20) and (21) (using the optimised coefficient values) are included in Figs. 7, 9, 10 and 11 for comparison with the 3D FEA calculations. In general, the predictions of Eqs. (20) and (21) agree reasonably well with the 3D FEA calculations, especially the salient features such as the size and shape of the local failure envelopes. Following the procedures detailed in Suryasentana et al. (2021), Eqs. (20) and (21) can be redefined in terms of the 6DoF soil reactions  $\{h_x, m_y, h_y, m_x, v, q\}$ . This is achieved by making the following replacements in Eq. (22): (i)  $\tilde{h}_i$  replaced by  $\sqrt{\tilde{h}_x^2 + \tilde{h}_y^2}$ , (ii)  $\tilde{m}_j$  replaced by  $\sqrt{\tilde{m}_x^2 + \tilde{m}_y^2}$ , and (iii)  $\tilde{h}_i \tilde{m}_j \cos \alpha_{hm'}$  replaced by  $\tilde{h}_y \tilde{m}_x - \tilde{h}_x \tilde{m}_y$ .

**Table 2**

Best-fit coefficients of the SOS-convex polynomials that make up the skirt failure envelope  $f^{\text{skirt}}$  in Eq. (22), as determined by the optimisation process in Eq. (6).

$p$	$a_1$	$a_2$	$a_3$	$a_4$	$a_5$	$a_6$	$a_7$	$a_8$	$a_9$	$a_{10}$
$p_1^{\text{skirt}}$	-0.93	0.65	-0.87	1.58	-2.42	5.66	0.3	-0.54	1.36	2.22
$p_2^{\text{skirt}}$	-1.36	1.71	-1.95	1.03	-4.06	5.17	0.2	-0.94	1.5	2.85

**Table 3**

Best-fit coefficients of the SOS-convex polynomials that make up the base failure envelope  $f^{\text{base}}$  in Eq. (23), as determined by the optimisation process in Eq. (6).

$p$	$a_1$	$a_2$	$a_3$	$a_4$	$a_5$	$a_6$	$a_7$	$a_8$	$a_9$	$a_{10}$
$p_1^{\text{base}}$	-0.36	0.9	-1.43	0.4	0.84	1.64	2.61	-0.84	0.34	0
$p_2^{\text{base}}$	-0.79	2.73	-1.13	0.88	0.31	0.88	2.55	-0.11	0.59	0

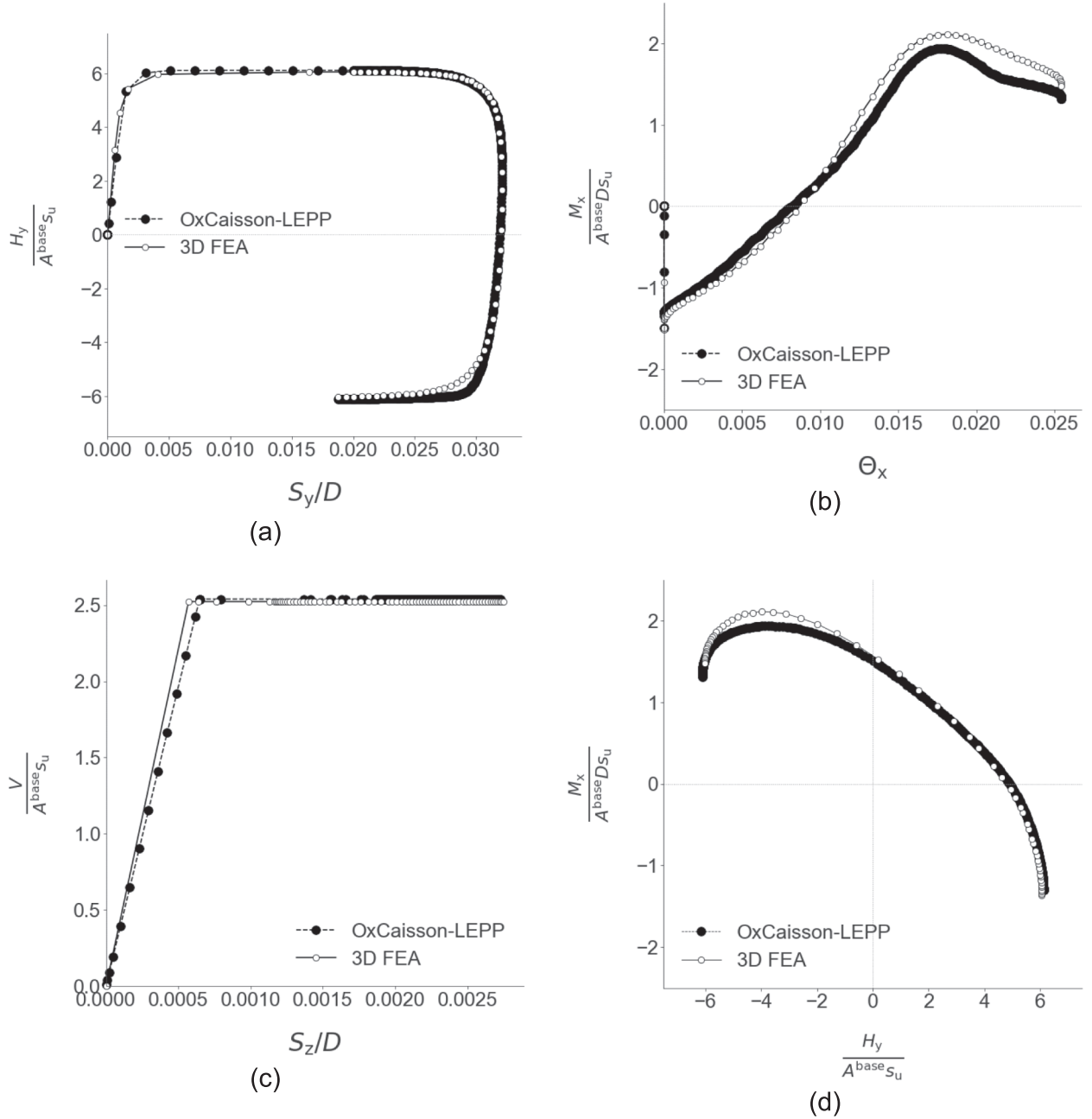


**Fig. 12.** Comparison of a sequential swipe test in the  $HM$  load space for a suction caisson of  $L/D = 0.5$  and for  $\alpha_{HM} = 0, \tilde{V} = 0.25, \tilde{Q} = 0$ . (a)-(c) Load-displacement behaviour (d)  $HM$  failure envelope.

### 3.7. Validation of OxCaisson-LEPP

Eqs. (20) and (21) are used as the yield functions and plastic potentials for the soil reactions in OxCaisson-LEPP. These formulations require the uniaxial capacities of the skirt and base soil reactions, which are defined in Eqs. (2)–(9). Fig. 12 compares the OxCaisson-LEPP predictions of the global load–displacement behaviour and *HM* failure envelopes for a caisson of  $L/D = 0.5$  with the 3D FEA results. In this figure, a sequential swipe test in the *HM* space under planar *HM* loading was carried out, with  $\tilde{V} = 0.25$  and  $\tilde{Q} = 0$ . Evidently, there is excellent agreement between the OxCaisson-LEPP predictions and the 3D FEA results. For further insights into the prediction of the *HM* failure envelope by OxCaisson-LEPP, Fig. 13 shows the history of the *H* and *M* loads and the corresponding *h* and *m* soil reactions. As the *HM* failure envelope is being explored, the skirt and base soil reactions travel along their respective yield surfaces. The predictions of OxCaisson-LEPP in Fig. 13 is very similar to that of the 3D FEA model in Fig. 6b. One of the main advantages of OxCaisson-LEPP is its efficiency. While the 3D FEA model took about 2 h to generate the data points in Fig. 12, OxCaisson-LEPP took about 2 min. This efficiency enables computationally intensive applications such as automated optimisation of suction caisson foundations (Suryasentana et al., 2019; Suryasentana et al., 2018).

To validate the ability of OxCaisson-LEPP to estimate the caisson capacity under non-planar *HM* loading and combined vertical and torsional loading, Fig. 14 shows the normalised  $H_x$ - $M_x$  and  $H_y$ - $M_x$  failure envelopes resulting from a sequential swipe test under non-planar *HM* loading with  $\tilde{V} = 0.5$  and  $\tilde{Q} = 0.25$ . It is evident that OxCaisson-LEPP is able to reproduce the 3D FEA results well.

### 3.8. Cowden till case study

To evaluate the hypothesis that OxCaisson-LEPP can be applied to a soil profile that differs from that used for calibration, OxCaisson-LEPP is used to estimate the planar *HM* failure envelope of a suction caisson of  $D = 10$  m and  $L = 12$  m, based on a real-world Cowden till undrained shear strength  $s_u$  profile (Zdravković et al., 2020) that varies irregularly with depth (see Fig. 15a). The OxCaisson-LEPP estimations will be compared with the calculations made by 3D FEA. Additionally, it would be informative to compare the OxCaisson-LEPP estimations with those by existing macro-element failure envelope models.

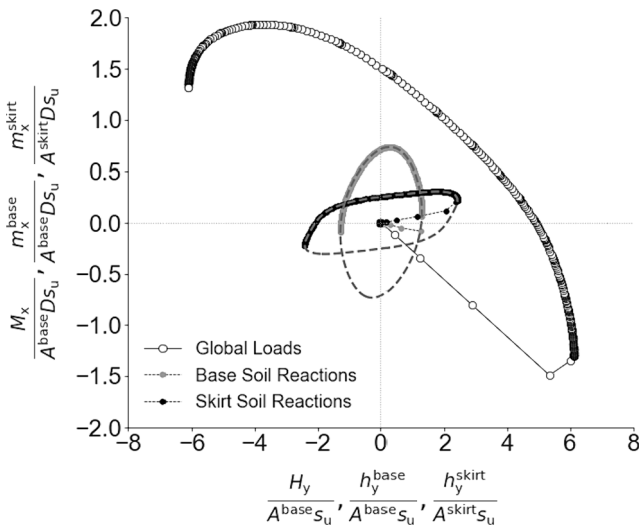
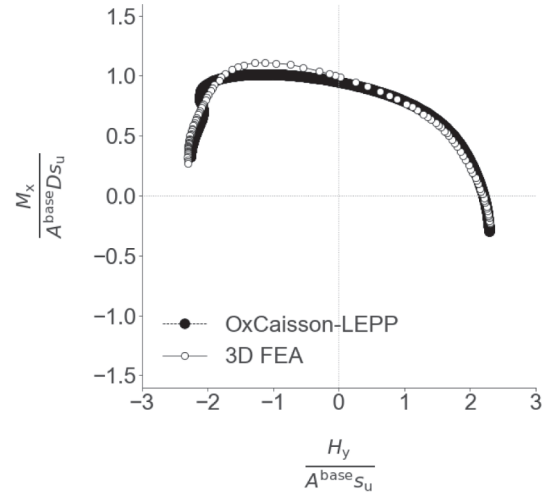
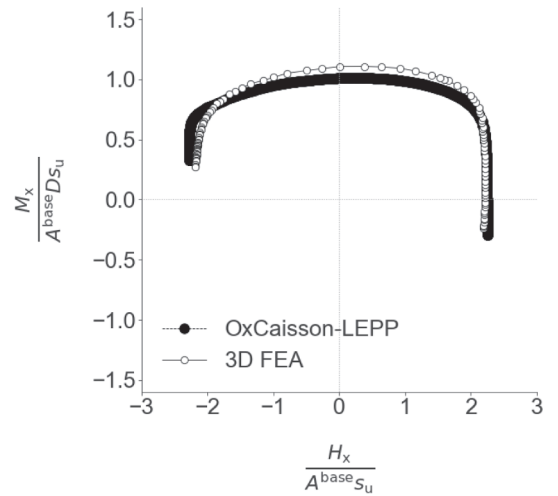


Fig. 13. Sequential swipe load history of the OxCaisson-LEPP predictions in the global *HM* and local *hm* spaces for a caisson of  $L/D = 0.5$ , for  $\alpha_{HM} = 0$ ,  $\tilde{V} = 0.25$ ,  $\tilde{Q} = 0$ . The grey dashed lines are the *hm* contours of the soil reaction failure envelopes predicted by Eqs. (20) and (21).



(a)



(b)

Fig. 14. Normalised  $H_y$ - $M_x$  and  $H_x$ - $M_x$  failure envelopes computed for a sequential swipe test on a caisson of  $L/D = 0.25$  under non-planar *HM* loading for  $\alpha_{SE} = \frac{\pi}{4}$ ,  $\tilde{V} = 0.5$ ,  $\tilde{Q} = 0.25$ .

However, it is quite challenging to find a suitable macro-element failure envelope model that can be applied to this routine *HM* failure envelope estimation task. The model proposed by Vulpe (2015) cannot be used as it has only been calibrated for a finite number of  $L/D$  ratios ( $L/D = 0, 0.1, 0.25, 0.5$ ). The model proposed by Liu et al. (2023) is calibrated only for undrained shear strength profiles in the form of  $s_u = kz$ , which cannot fit well with the data presented in Fig. 15a. Given these limitations, the most compatible among the existing models, proposed by Hung and Kim (2014), is used to estimate the *HM* failure envelope. To use this model, a representative design  $s_u$  profile has to be first fitted to the irregular profile based on the parametric form  $s_u = s_{um} + kz$ , which was used to calibrate the model; this process is not straightforward for the profile in Fig. 15a and can be very subjective, introducing additional uncertainty to the design outcomes.

A design profile ( $s_u = 85 + 5.5z$  kPa) was adopted to capture the major trend of the  $s_u$  profile, as shown in Fig. 15a. Based on this design profile, the caisson failure envelope estimated by Hung and Kim (2014) is,

$$f(\tilde{H}, \tilde{M}, \tilde{V}) = \tilde{M}^2 + \alpha\beta\lambda\tilde{H}\tilde{M} + \tilde{H}^2 + \tilde{V}^2 - 1 = 0 \quad (23)$$



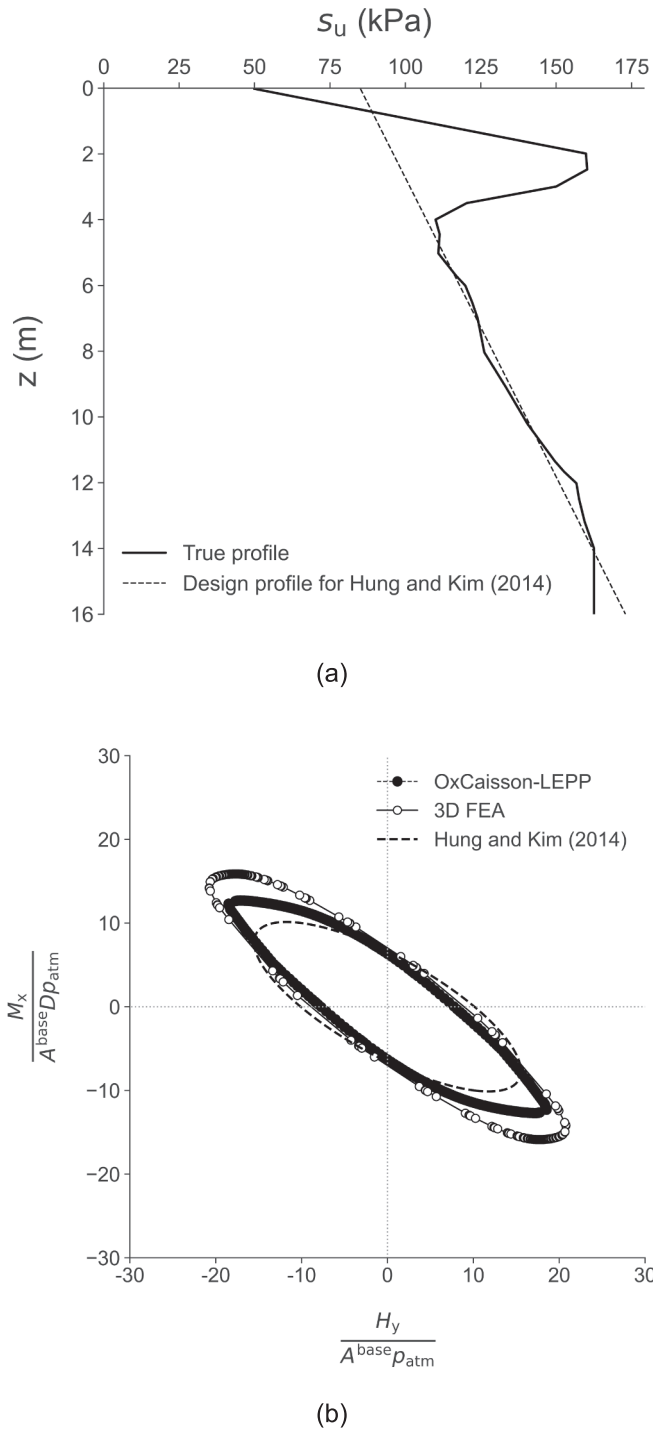


**Fig. 15.** (a) Undrained shear strength profile of Cowden Till site (b) Comparison of the OxCaisson-LEPP and 3D FEA predictions for the normalised planar HM failure envelope of a caisson of  $D = 10$  m and  $L/D = 1.2$ , where  $p_{atm}$  is the atmospheric pressure.

where  $\alpha = 0.323$ ,  $\beta = 5$  and  $\lambda = 0.94$ .

Fig. 15b compares the HM failure envelopes calculated by OxCaisson-LEPP, Hung and Kim (2014) and 3D FEA. The OxCaisson-LEPP calculations agree reasonably well with the 3D FEA calculations, with some underestimation of the capacity, especially towards the extremes of the  $H$  and  $M$  loads. In comparison to the model by Hung and Kim (2014), the OxCaisson-LEPP calculations exhibit a closer match to the 3D FEA calculations; this is despite the Hung and Kim (2014) model

being calibrated using a linearly increasing  $s_u$  profile that is more similar to Fig. 15a than the uniform  $s_u$  profile that was used to calibrate OxCaisson-LEPP.

#### 4. Discussion

The current paper addresses two key gaps in understanding and modelling the ultimate behaviour of suction caissons in undrained clay. First, it examines the local soil response on caissons at capacity under combined 6DoF loading; the interaction between the various soil reaction components (e.g. interaction between horizontal and moment soil reactions) at capacity is identified. It is shown that the uniaxial capacity of the base soil reactions stops increasing after  $L/D > 1$ ; this indicates that the relative importance of the base soil reactions diminishes as  $L/D$  increases. Second, the paper proposes an elastoplastic Winkler model for estimating the failure envelopes for caissons under combined 6DoF loading. Previous research in this area is limited, particularly in connection with the estimation of failure envelopes for non-planar HM loading which is important for offshore wind applications due to the different directions of wind and wave actions.

Despite the simplifying assumption of independent skirt soil reactions (i.e., the skirt soil reactions at one depth do not interact with the skirt soil reactions at other depths), the Winkler model offers a more versatile framework than traditional macro-element models. Macro-element models are typically applicable only for the specific soil profiles that they were calibrated for; this limits their usefulness for general design applications. This is evident in the Cowden till case study presented in the paper, where only one of the reviewed macro-element models (Hung and Kim, 2014) appears to be applicable; in all other cases the Cowden till soil profile differs significantly from the soil profiles used to calibrate the macro-element models.

The Winkler model employed in the current work is capable of conducting design calculations for actual design soil profiles; this contrasts with macro-element models for which idealised soil profiles – to approximate actual site conditions – need to be adopted. Macro-element models therefore require an additional, subjective, step of determining a representative soil profile from the actual site data; this adds uncertainty to the design outcomes. Therefore, a key advantage of Winkler-based models such as OxCaisson-LEPP is that it can be used directly for sites with irregular undrained shear strength profiles.

The success of Winkler modelling for caissons has been noted in other studies, such as those by Antoniou et al. (2022). The efficacy of Winkler modelling for low  $L/D$  caisson-like structures is also demonstrated by the PISA design model (Burd et al., 2020), which is applicable to piles with  $L/D = 2$ ; this is close to typical aspect ratios for caissons.

This paper focuses on estimating the failure envelopes for caissons in undrained clay; this is crucial for assessing the ultimate limit state conditions for foundations, especially in the context of caisson-based anchoring systems. However, there are other factors such as foundation stiffness and cyclic behaviour that could significantly influence the design of a caisson in actual design cases. The issue of foundation stiffness has been explored in previous studies (e.g. Suryasentana et al., 2022,2023a,2023b). The issue of cyclic behaviour under combined loading, however, is complex and is planned for future research.

#### 5. Conclusions

This paper carries out an extensive 3D FEA study to investigate the ultimate response of the local soil reactions acting on a suction caisson in undrained clay under combined 6DoF loading. The 3D FEA results show the interaction paths of the skirt and base soil reactions at capacity, which approximate soil reaction failure envelopes. SOS-convex polynomial-based formulations are derived to approximate these soil reaction failure envelopes. A new elastoplastic Winkler model called OxCaisson-LEPP was developed, with the derived skirt and base failure envelope formulations acting as the yield functions and plastic

potential for the soil reactions of the model. The results show that Ox-Caisson-LEPP can accurately reproduce the 3D FEA results with high efficiency, even for soil profiles that differ from that used to calibrate the model.

### CRedit authorship contribution statement

**Stephen K. Suryasentana:** Conceptualization, Data curation, Formal analysis, Investigation, Methodology, Software, Writing – original draft. **Harvey J. Burd:** . **Byron W. Byrne:** . **Avi Shonberg:** Methodology, Supervision, Writing – review & editing.

### Declaration of competing interest

The authors declare that they have no known competing financial interests or personal relationships that could have appeared to influence the work reported in this paper.

### Data availability

Data will be made available on request.

### Acknowledgments

Part of this work was completed during the DPhil studies of the first author and he would like to acknowledge the generous support of Ørsted Wind Power for funding his DPhil studentship at the University of Oxford. Byrne is supported by the Royal Academy of Engineering under the Research Chairs and Senior Research Fellowships scheme.

### References

- Antoniou, M., Kourkoulis, R., Gelagoti, F., Anastasopoulos, I., 2022. Simplified method for performance-based seismic design of suction caissons supporting jacket offshore wind turbines. *Soil Dyn. Earthq. Eng.* 155, 107169.
- API, 2011. Recommended Practice 2GEO Geotechnical and Foundation Design Considerations. American Petroleum Institute, Washington (DC, USA).
- Boyd, S., Vandenberghe, L., 2004. *Convex optimization*. Cambridge University Press.
- Bransby, M.F., Randolph, M.F., 1998. Combined loading of skirted foundations. *Géotechnique* 48 (5), 637–655.
- Bransby, M.F., Randolph, M.F., 1999. The effect of embedment depth on the undrained response of skirted foundations to combined loading. *Soils Found.* 39 (4), 19–33.
- Bransby, M.F., Yun, G.J., 2009. The undrained capacity of skirted strip foundations under combined loading. *Géotechnique* 59 (2), 115–125.
- Burd, H.J., Taborda, D.M., Zdravković, L., Abadie, C.N., Byrne, B.W., Housby, G.T., Gavin, K.G., Igoe, D.J., Jardine, R.J., Martin, C.M., McAdam, R.A., 2020. PISA design model for monopiles for offshore wind turbines: application to a marine sand. *Géotechnique* 70 (11), 1048–1066.
- Butterfield, R., Housby, G.T., Gottardi, G., 1997. Standardized sign conventions and notation for generally loaded foundations. *Géotechnique* 47 (5), 1051–1054.
- Byrne, B.W., Aghakouchak, A., Buckley, R.M., Burd, H.J., Gengenbach, J., Housby, G.T., McAdam, R.A., Martin, C.M., Schranz, F., Sheil, B.B. and Suryasentana, S.K., (2020b). PICASO: Cyclic lateral loading of offshore wind turbine monopiles. In *Frontiers in Offshore Geotechnics IV: Proceedings of the 4th International Symposium on Frontiers in Offshore Geotechnics (ISFOG 2021)*.
- Byrne, B.W., Housby, G.T., Burd, H.J., Gavin, K.G., Igoe, D.J., Jardine, R.J., Martin, C.M., McAdam, R.A., Potts, D.M., Taborda, D.M., Zdravković, L., 2020. PISA design model for monopiles for offshore wind turbines: application to a stiff glacial clay till. *Géotechnique* 70 (11), 1030–1047.
- Dassault Systèmes, 2014. *Abaqus User Manual*. Simula Corp, Providence, RI.
- Doherty, J.P., Housby, G.T., Deeks, A.J., 2005. Stiffness of flexible caisson foundations embedded in nonhomogeneous elastic soil. *J. Geotech. Geoenviron. Eng.* 131 (12), 1498–1508. [https://doi.org/10.1061/\(ASCE\)1090-0241\(2005\)131:12\(1498\)](https://doi.org/10.1061/(ASCE)1090-0241(2005)131:12(1498)).
- Efthymiou, G., Gazetas, G., 2019. Elastic stiffnesses of a rigid suction caisson and its cylindrical sidewall shell. *J. Geotech. Geoenviron. Eng.* 145 (2), 06018014. [https://doi.org/10.1061/\(ASCE\)GT.1943-5606.0002013](https://doi.org/10.1061/(ASCE)GT.1943-5606.0002013).
- Feng, X., Randolph, M.F., Gourvenec, S., Wallerand, R., 2014a. Design approach for rectangular mudmats under fully three-dimensional loading. *Géotechnique* 64 (1), 51–63.
- Feng, X., Gourvenec, S., Randolph, M.F., 2014b. Optimal skirt spacing for subsea mudmats under loading in six degrees of freedom. *Appl. Ocean Res.* 48, 10–20.
- Feng, X., Gourvenec, S., 2015. Consolidated undrained load-carrying capacity of subsea mudmats under combined loading in six degrees of freedom. *Géotechnique* 65 (7), 563–575.
- Feng, X., Gourvenec, S., Randolph, M.F., Wallerand, R., Dimmock, P., 2015. Effect of a surficial crust on mudmat capacity under fully three-dimensional loading. *Géotechnique* 65 (7), 590–603.
- Gourvenec, S., Barnett, S., 2011. Undrained failure envelope for skirted foundations under general loading. *Géotechnique* 61 (3), 263–270.
- He, R., Pak, R.Y.S., Wang, L.Z., 2017. Elastic lateral dynamic impedance functions for a rigid cylindrical shell type foundation. *Int. J. Numer. Anal. Meth. Geomech.* 41 (4), 508–526. <https://doi.org/10.1002/nag.2567>.
- Hung, L.C., Kim, S., 2014. Evaluation of Undrained Bearing Capacities of Bucket Foundations Under Combined Loads. *Mar. Georesour. Geotechnol.* 32 (1), 76–92.
- ISO, 2016. ISO 19901–4: Petroleum and Natural Gas Industries Specific Requirements for Offshore Structures – Part 4: Geotechnical and Foundation Design Considerations, second ed. International Standards Organisation, Geneva, Switzerland.
- Jalbi, S., Shadlou, M., Bhattacharya, S., 2018. Impedance functions for rigid skirted caissons supporting offshore wind turbines. *Ocean Eng.* 150 (Feb), 21–35.
- Liu, T., Zhang, Y., Meng, Q., 2023. Numerical investigation and design of suction caisson for on-bottom pipelines under combined VHMT loading in normal consolidated clay. *Ocean Eng.* 274, 113997.
- Löfberg, J., 2009. Pre- and post-processing sum-of-squares programs in practice. *IEEE Trans. Autom. Control* 54 (5), 1007–1011.
- Löfberg, J. (2004). YALMIP: a toolbox for modeling and optimization in MATLAB. In: '2004 IEEE International Conference on Robotics and Automation', IEEE. pp. 284–289.
- Offshore Wind Accelerator, 2019. *Suction Installed Caisson Foundations for Offshore Wind: Design Guidelines*. Carbon Trust.
- Paikowsky, S.G., 2010. LRFD design and construction of shallow foundations for highway bridge structures, vol. 651. Transportation Research Board.
- Shen, Z., Bie, S., Guo, L., 2017. Undrained capacity of a surface circular foundation under fully three-dimensional loading. *Comput. Geotech.* 92, 57–67.
- Suryasentana, S. K., and Lehane, B. M. (2014b). Verification of numerically derived CPT based py curves for piles in sand. In: *Proceedings of 3rd International Symposium on Cone Penetration Testing* (pp. 3–29). Las Vegas, Nevada USA.
- Suryasentana, S.K., Burd, H.J., Byrne, B.W., Shonberg, A., 2020a. A systematic framework for formulating convex failure envelopes in multiple loading dimensions. *Géotechnique* 70 (4), 343–353.
- Suryasentana, S., Byrne, B., Burd, H., 2019. Automated optimisation of suction caisson foundations using a computationally efficient elastoplastic Winkler model. *Coastal Struct.* 2019, 932–941.
- Suryasentana, S.K., Housby, G.T., 2022. A Convex Modular Modelling (CMM) framework for developing thermodynamically consistent constitutive models. *Comput. Geotech.* 142, 104506.
- Suryasentana, S.K., Lehane, B.M., 2014a. Numerical derivation of CPT-based p–y curves for piles in sand. *Géotechnique* 64 (3), 186–194.
- Suryasentana, S.K., Lehane, B.M., 2016. Updated CPT-based p–y formulation for laterally loaded piles in cohesionless soil under static loading. *Géotechnique* 66 (6), 445–453.
- Suryasentana, S.K., Mayne, P.W., 2022. Simplified method for the lateral, rotational, and torsional static stiffness of circular footings on a nonhomogeneous elastic half-space based on a work-equivalent framework. *J. Geotech. Geoenviron. Eng.* 148 (2), 04021182.
- Suryasentana, S.K., Dunne, H.P., Martin, C.M., Burd, H.J., Byrne, B.W., Shonberg, A., 2020b. Assessment of numerical procedures for determining shallow foundation failure envelopes. *Géotechnique* 70 (1), 60–70.
- Suryasentana, S.K., Burd, H.J., Byrne, B.W., Shonberg, A., 2021. Automated procedure to derive convex failure envelope formulations for circular surface foundations under six degrees of freedom loading. *Comput. Geotech.* 137, 104174.
- Suryasentana, S.K., Burd, H.J., Byrne, B.W., Shonberg, A., 2022. A Winkler model for suction caisson foundations in homogeneous and non-homogeneous linear elastic soil. *Géotechnique* 72 (5), 407–423.
- Suryasentana, S.K., Burd, H.J., Byrne, B.W., Shonberg, A., 2023a. Modulus weighting method for static stiffness estimations of suction caisson foundations in layered soil conditions. *Géotechnique Lett.* 1–21.
- Suryasentana, S.K., Burd, H.J., Byrne, B.W., Shonberg, A., 2023b. Small-strain, non-linear elastic Winkler models for uniaxial loading of suction caisson foundations. *Géotechnique Lett.* 13 (3), 1–12.
- Suryasentana, S. K., Byrne, B. W., Burd, H. J., and Shonberg, A. (2017). Simplified model for the stiffness of suction caisson foundations under 6DoF loading. In *Proceedings of SUT OSIG 8th International Conference*, 554–561. London, UK. <https://doi.org/10.3723/OSIG17.554>.
- Suryasentana, S. K., Byrne, B. W., Burd, H. J., and Shonberg, A. (2018). An elastoplastic 1D Winkler model for suction caisson foundations under combined loading. *Numerical Methods in Geotechnical Engineering IX*, 973–980. CRC Press.
- Vulpe, C., 2015. Design method for the undrained capacity of skirted circular foundations under combined loading: effect of deformable soil plug. *Géotechnique* 65 (8), 669–683.
- Zdravković, L., Taborda, D.M., Potts, D.M., Abadias, D., Burd, H.J., Byrne, B.W., Gavin, K.G., Housby, G.T., Jardine, R.J., Martin, C.M., McAdam, R.A., 2020. Finite-element modelling of laterally loaded piles in a stiff glacial clay till at Cowden. *Géotechnique* 70 (11), 999–1013.